Stem Cell Reports
Article

ISSCR

OPEN ACCESS

Development and Dynamic Regulation of Mitochondrial Network in Human Midbrain Dopaminergic Neurons Differentiated from iPSCs

Du Fang,[1,3] Yu Qing,[1,2,3] Shijun Yan,[1] Doris Chen,[1] and Shirley ShiDu Yan[1,*]
[1]Department of Pharmacology and Toxicology, Higuchi Bioscience Center, School of Pharmacy, University of Kansas, 2099 Constant Avenue, Lawrence, KS 66047, USA
[2]State Key Laboratory of Oral Diseases, West China Hospital of Stomatology, Sichuan University, Cheng Du 610041, China
[3]Co-first author
*Correspondence: shidu@ku.edu
http://dx.doi.org/10.1016/j.stemcr.2016.08.014

SUMMARY

Mitochondria are critical to neurogenesis, but the mechanisms of mitochondria in neurogenesis have not been well explored. We fully characterized mitochondrial alterations and function in relation to the development of human induced pluripotent stem cell (hiPSC)-derived dopaminergic (DA) neurons. Following directed differentiation of hiPSCs to DA neurons, mitochondria in these neurons exhibit pronounced changes during differentiation, including mature neurophysiology characterization and functional synaptic network formation. Inhibition of mitochondrial respiratory chains via application of complex IV inhibitor KCN (potassium cyanide) or complex I inhibitor rotenone restricted neurogenesis of DA neurons. These results demonstrated the direct importance of mitochondrial development and bioenergetics in DA neuronal differentiation. Our study also provides a neurophysiologic model of mitochondrial involvement in neurogenesis, which will enhance our understanding of the role of mitochondrial dysfunctions in neurodegenerative diseases.

INTRODUCTION

Human induced pluripotent stem cells (hiPSCs) are remarkable for their ability to self-renew and differentiate into various tissues and cell types (Takahashi and Yamanaka, 2006). Differentiation of these cells into a specific cell type allows for in-depth study with the goal of cell replacement therapy for neurodegenerative diseases such as Parkinson's disease (PD), which is caused by selective loss of dopaminergic (DA) neurons in the substantia nigra pars compacta in the midbrain (Xu et al., 2013b). Expanding our knowledge of the cellular and molecular factors involved in the maturation and differentiation of human-derived neurons will significantly boost our ability to manipulate and generate specific cell types for disease therapy.

Mitochondria are highly dynamic organelles with complex structures involved in multiple processes, including energy metabolism, reactive oxygen species (ROS) generation, mitochondrial dynamics and distribution, and the induction of apoptosis. A number of recent studies have highlighted the key role of mitochondrial biogenesis in stem cell differentiation (Prigione et al., 2011; Teslaa and Teitell, 2015; Xu et al., 2013a). Upregulation of mitochondrial mass and mtDNA and increased oxygen consumption levels were observed during differentiation of embryonic stem cells (ESCs) (Prigione et al., 2011). In addition, mitochondria gained structural maturity, displaying larger morphology during differentiation (Bukowiecki et al., 2014). This morphologic change was accompanied by a metabolic transition from glycolysis to mitochondrial respiration in both cardiac and motor-neuronal directional differentiation (O'Brien et al., 2015). Inhibition of mitochondrial respiration leads to the impairment of differentiation ability and enhancement of stem cell pluripotency (Varum et al., 2009). Thus, the development of a mature mitochondrial network in terms of mitochondrial function and structure is necessary during the differentiation of PSCs.

Mitochondrial dysfunction occurs in a wide variety of degenerative diseases such as aging, cancer, and neurodegenerative diseases (Mattson et al., 2008; Perier and Vila, 2012). Mitochondrial ROS (mROS) levels are tightly regulated and linked to a wide range of physiologic processes (Genova et al., 2004). mROS are also involved in cellular processes that are critical for maintenance of homeostasis and adaptation to stress (Chandel et al., 1998). Recent studies showed that human ESCs maintain their genomic integrity by limiting the accumulation of ROS (Armstrong et al., 2010; Asensi et al., 2014), However, overproduction of mROS has adverse effects on cellular function including that of PSCs (Genova et al., 2004; Sena and Chandel, 2012; Tapia, 2006; Wu et al., 2013). In hiPSC-induced neurons derived from PD patients, mitochondrial dysfunction and high levels of ROS result in increased vulnerability of these cells (Cooper et al., 2012). Mechanisms underlying mitochondrial defects in hiPSC-derived tyrosine hydroxylase (TH)-positive DA neurons are not well understood.

To better understand the role of mitochondria in the development and differentiation process of hiPSCs into DA neurons, we evaluated changes in mitochondrial dynamics and function in DA neurons during various phases

of differentiation. We fully characterized and evaluated the neurophysiology, morphology, and neuronal and synaptic markers to monitor maturation and synaptic activity in hiPSC-derived DA neurons. Importantly, interruption of mitochondrial respiration by inhibiting complex IV or I activity significantly obstructed the differentiation of DA neurons. Our current study clearly demonstrated the importance of mitochondria in DA neuronal differentiation and maturation. We therefore provide a dynamic model for further investigation of the involvement of mitochondrial dysfunction in the development of neurodegenerative diseases.

RESULTS

hiPSC Characterization and DA Neuron-Directed Differentiation

We first assessed pluripotency in bone marrow 2-3 (BM2-3) hiPSCs. These cells were immunoreactive for pluripotency markers NANOG, OCT4, SSEA3, and SOX2 (Figure S1A). Our iPSCs were successfully kept in an undifferentiated state for more than 20 passages. The cells formed uniform-sized embryoid bodies (EBs) 24 hr after being plated into AggreWell800 plates (Figure S1B). One to two days after attachment of EBs, prominent neural rosette structures appeared in neural aggregates with the addition of Rock inhibitor (Y27632). About 98% of attached neural aggregates had polarized rosettes covering >50% of their area. Rosettes were formed by cells expressing proteins characteristic of progenitor markers of PAX6 (green) and Ki-67 (red) (Figure S1C, and immunoblot results in Figure S1D). Dachshund family transcription factor 1 (DACH1) and promyelocytic leukemia zinc finger expressions from our semi-quantitative PCR results confirmed the neural rosette characteristics (Figure S1E). Endogenous pluripotency marker OCT4 and progenitor marker PAX6 were downregulated in differentiated neurons kept in the DA neuronal differentiation medium for 10, 15, and 20 days, whereas expression levels of mature neuron-specific marker TUJ1 (neuron-specific class III β-tubulin) and DA neuron marker TH were significantly increased during these same periods of time (Figures 1A–1E).

Real-time qPCR results showed that the mRNA for earlier markers expressed in midbrain dopaminergic neuron progenitors or immature dopaminergic neurons, including *LIM-homeobox transcription factor 1 alpha*, *LMX1A*, and *Engrailed 1* (*EN1*); a basal and floorplate marker (*Forkhead Box A2*, *FOXA2*) (Nakatani et al., 2010), and a transcription factor, expressed at the rostral to midbrain/hindbrain boundary, *Orthodenticle Homeobox 2* (*OTX2*) (Millet et al., 1996). These reached a plateau at the stage of neural progenitor cells (NPCs) (Figure 1F).

In contrast, the mRNA levels of *dopamine transporter* (*DAT*), *aromatic L-amino acid decarboxylase* (*AADC*), and *vesicular monoamine transporter 2* (*VMAT2*), markers of mature DA neurons (Bjorklund et al., 2002; Kim et al., 2011), and the marker for mature neurons, *microtubule-associated protein 2* (*MAP2*), are increased over time during dopaminergic neuron induction (Figure 1F).

We observed significant growth of dendrites with the longest processes noted on day 20 as measured by TUJ1- or TH-positive process length during the course of differentiation (Figures 1G and 1H). These data indicate that DA neurons can be induced to display mature neuronal characteristics in our differentiation system directed at DA neurons.

Physiological Characteristics of Differentiated DA Neurons

To further determine whether DA neurons derived from differentiated hiPSCs actually have a neurophysiologic function, we next examined the electrophysiologic properties of hiPSC-induced DA neurons. During differentiation, the ability to fire bursts of action potentials in response to current injection increased over time (Figures 2A and 2B). None of the neurons exhibited action potentials until day 10 of the incubation in DA differential media when a single potential appeared (Figure 2B). The frequency continued to increase up to day 20 (Figures 2A and 2B). Electrophysiological parameters such as resting membrane potential and action potential generation showed signs of membrane maturation over time (Figures 2A and 2B). Four cells (1.7%, n = 242) showed spontaneous action potentials, some appearing as early as 15 days after induction (Figure 2C). We were able to block the action potentials with the addition of tetrodotoxin (TTX), a specific inhibitor of Na^+ ion channels (Figure 2D, upper panel).

Whole-cell patch-clamp recordings from individual cells revealed the presence of voltage-gated sodium currents and voltage-gated potassium currents in hiPSC-derived DA neurons; these increased over the time of induction (Figure 2C). In voltage-clamp mode, we observed fast inactivating inward and outward currents, which probably correspond to the opening of voltage-dependent Na^+ and K^+ channels, respectively. The fast inward currents were reversibly blocked with the addition of TTX (Figure 2D, upper panel) and the outward currents were reversibly blocked by tetraethylammonium, an inhibitor of voltage-dependent K^+ channels (Figure 2D, lower panel). Na^+ and K^+ channels also showed signs of maturation over time of induction (Figures 2C–2E). Taken together, these data demonstrate that hiPSC-derived DA neurons are functional after 15 days of differentiation in our DA neuron induction system.

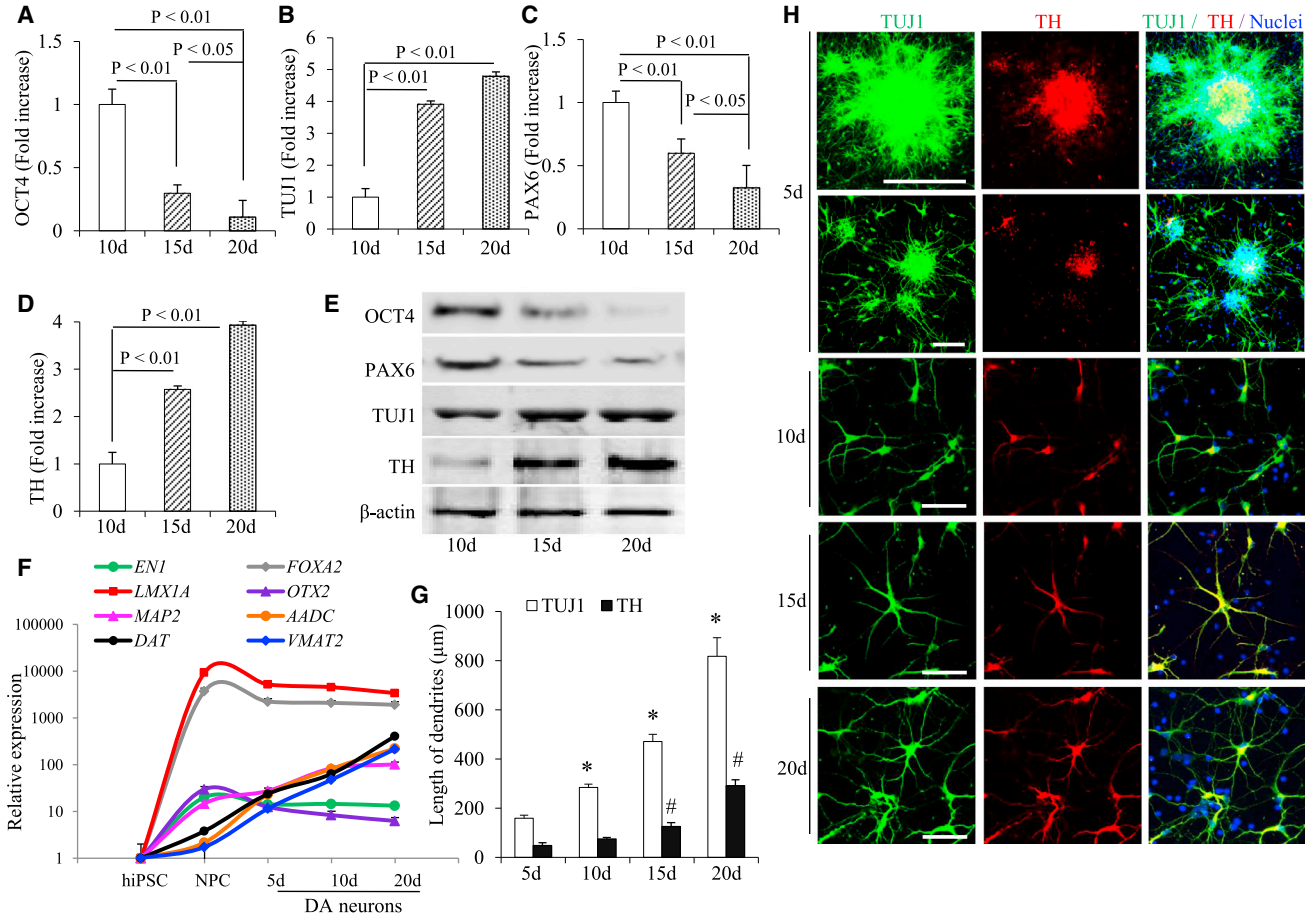

Figure 1. Differentiation and Development of hiPSC Line-Induced Human DA Neurons

(A–E) Expression of pluripotency marker (OCT4), precursor cells marker (PAX6), neuron-specific marker (neuron-specific class III β-tubulin, TUJ1), and midbrain dopaminergic neuronal marker (TH) in neuronal populations in differentiation media for 10, 15, and 20 days. (A–D) Densitometry of the combined immunoreactive bands for OCT4 (A), PAX6 (B), TUJ1 (C), and TH (D) normalized to β-actin using NIH ImageJ software. Data are expressed as fold increase relative to DA neurons cultured in differentiation media for 10 days (n = 3 independent experiments; mean ± SEM). (E) Representative immunoblots for OCT4, PAX6, TUJ1, TH, and β-actin. β-Actin was used as a protein loading control.

(F) Real-time qPCR results for gene expression. The expression level of the undifferentiated hiPSC cells was set to 1 (n = 3 independent experiments).

(G and H) Co-expression of TUJ1 and TH in hiPSC-induced neurons cultured in differentiation media for 5, 10, 15, and 20 days. Quantification of neuronal process length of TUJ1-positive neurons and TH-positive DA neurons in differentiation media for different days was performed using NIH ImageJ (G). $^{\#}p < 0.01$ compared with day-5 (5d) cells, length of TUJ1 positive dendrites, and $^{*}p < 0.01$ compared with 5d cells, length of TH positive dendrites (n = 3 independent experiments; mean ± SEM, with 10 cells quantified per experiment). (H) Representative images for immunostaining of TUJ1 (green), TH (red), and co-localization (merge, yellow). Scale bars, 50 μm.

For (A), (D), and (G), statistical analysis was performed using StatView software version 5.0.1 (SAS Institute). One-way ANOVA was used for repeated-measures analysis, followed by Fisher's protected least significant difference for post hoc comparisons. Data are presented as mean ± SEM. Three independent experiments in (A–H); n = 10 cells per group per experiment in (G).

Formation of Functional Excitatory Synapses in hiPSC Differentiated DA Neurons

Synaptogenesis is a critical indicator of neural network formation. Using immunocytochemistry, we demonstrated that the number of synaptophysin (SYN)-positive puncta was significantly increased in day-15 to day-20 DA neurons compared with day-10 DA neurons (Figures 2F and 2G). There was an abundance of pre-synaptic compartments (SYN-positive puncta) localized along the dendrites of TH-positive DA neurons that were differentiated for a period of 20 days (Figure 2F), whereas SYN-positive puncta were barely detectable in the DA neurons that were

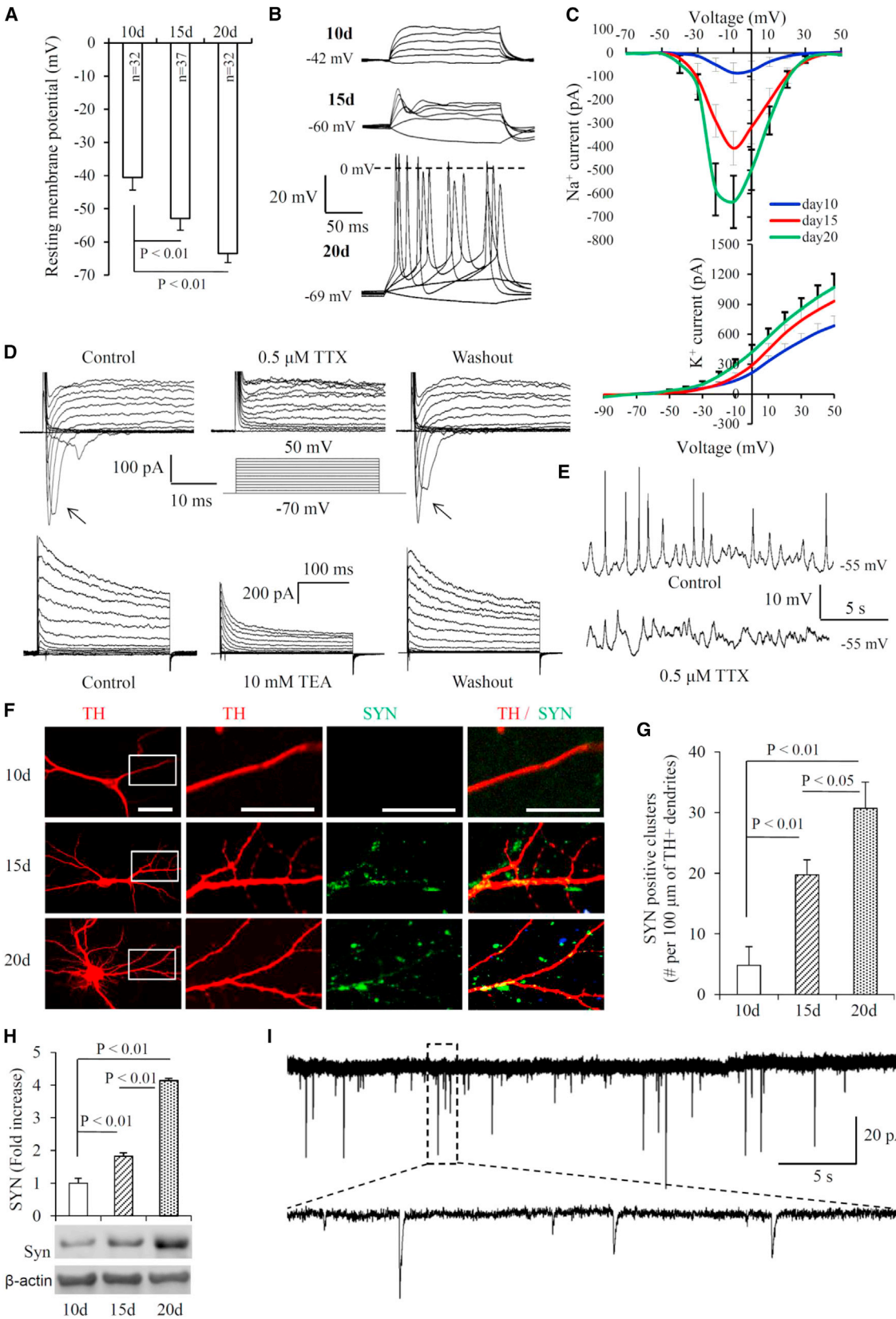

(legend on next page)

differentiated for 10 days. Consistent with the immunostaining results, SYN protein expression levels were elevated over the time of induction (Figure 2H).

We next performed a whole-cell patch-clamp recording to detect spontaneous postsynaptic currents (sPSCs) in the day-20 neurons to assess their neuronal function. As shown in Figure 2I, sPSCs with 10- to 60-pA amplitudes occurred frequently. Fourteen cells (5.8%, n = 242) exhibited the presence of sPSCs, suggesting that hiPSCs have the capacity to form functional synapses. These data demonstrate that functional and excitatory synapses are generated during the course of differentiation.

Alteration of Mitochondrial Function in hiPSC Differentiated DA Neurons

We next estimated mitochondrial potential and integrity of iPSC-induced DA neurons by assessing their ability to incorporate the mitochondrial membrane-permeable fluorescent dye tetramethylrhodamine methyl ester (TMRM), which is readily sequestered by active mitochondria. Mitochondrial membrane potential was significantly increased 1.6-, 2.3-, and 2.6-fold in day-10, -15, and -20 DA neurons, respectively (Figures 3A and 3B).

Given the important role of mitochondria in neuronal transmission and function, we next evaluated mitochondrial respiratory function and energy metabolism. We measured enzymatic activity for complexes I and IV, key enzymes associated with the respiratory chain, and ATP levels in hiPSC-derived DA neurons. Complex I and IV activity was significantly increased on day 20, compared with day-10 and -15 differentiated neurons (Figures 3C and 3D). Similarly, ATP levels were significantly elevated on day 15–20 compared with those from day 10 (Figure 3E). These results suggest enhanced mitochondrial respiratory chain function and energy metabolism during the course of maturation of hiPSC-DA neurons, which could result in increased mitochondrial membrane potential.

Overproduction of mitochondria-produced ROS is damaging to the cell, thereby accelerating pathologies and aging (Cooper et al., 2012). Recent work has revealed that mitochondrial ROS are integral signaling molecules that promote proliferation, and possibly also control differentiation (Chandel et al., 1998; Sena and Chandel, 2012; Tapia, 2006). We therefore assessed mitochondrial ROS levels by evaluating MitoSOX staining intensity in the neuronal terminals upon differentiation. The intensity of MitoSOX signals was increased in day-10, -15, and -20 differentiated DA neurons (Figures 3F and 3G). To further confirm the increased ROS levels during differentiation, we quantitatively measured the intracellular ROS levels by highly specific election paramagnetic resonance (EPR) spectroscopy. Compared with day 5 of differentiated DA neurons, the intracellular ROS levels were elevated at days 10, 15, and 20 of differentiated DA neurons (Figures 3H and 3I). Both mitochondrial ROS levels and mitochondrial function were highest on day 20 of differentiation.

Figure 2. Electrophysiologic Characterization of Maturation of hiPSC-Derived DA Neurons

(A) Quantification of resting membrane potential in hiPSC-derived DA neurons cultured in differentiation media for 10, 15, and 20 days. Numbers in the bars represent the numbers of recorded cells (n = 3 independent experiments; mean ± SEM).

(B) Representative traces of membrane potential responding to step depolarization by current injections ranging from −10 pA to 90 pA at 20-pA increments. Membrane potential was current-clamped at the resting membrane potential.

(C) Quantification of Na^+ and K^+ currents recorded from DA neurons at indicated days after differentiation. (n = 3 independent experiments with 13–16 cells per group in Na^+ currents record, 15 cells per group in K^+ currents record; mean ± SEM).

(D) Representative traces of Na^+ currents (upper panel) and K^+ currents (lower panel) in voltage-clamp mode; cells were held at −70 mV; step depolarization from −70 mV to +50 mV at 10-mV increments were delivered (lower panel). Na^+ currents and K^+ currents recorded from DA neurons were blocked by 0.5 μM tetrodotoxin (TTX) and 10 mM tetraethylammonium (TEA), respectively. Both currents recovered following TTX or TEA washout.

(E) TTX-sensitive spontaneous action potentials recorded from a DA neuron 20 days after differentiation. No current injection was applied.

(F) Immunocytochemistry of synaptophysin (SYN, marker for synaptic terminals, green) and TH (red). Scale bars, 20 μm.

(G) Quantification of numbers of SYN-positive clusters along the branches of hiPSC-derived DA neurons (TH-positive dendrites) cultured in differentiation media for 10, 15, and 20 days (n = 3 independent experiments; mean ± SEM, with 4 cells quantified per experiment).

(H) Analysis of western blots for Syn protein expression. Quantification of SYN expression level is shown in the upper panel. Data are normalized to the expression level of internal control β-actin (n = 3 independent experiments; mean ± SEM). Representative images are shown for SYN and β-actin in the lower panel.

(I) Representative spontaneous postsynaptic currents (sPSCs) recorded from hiPSC-derived DA neurons cultured in differentiation media for 20 days.

Statistical analysis was performed using StatView version 5.0.1. For (A), (G), and (H), one-way ANOVA was used for repeated-measures analysis, followed by Fisher's protected least significant difference for post hoc comparisons. Data are presented as mean ± SEM. Three independent experiments in (A), (C), (G), and (H); n = 32–37 cells per group in (A). In (C), n = 13–16 cells per group in Na^+ currents record, and n = 15 cells per group in K^+ currents record. In (G), n = 4 cells per group per experiment.

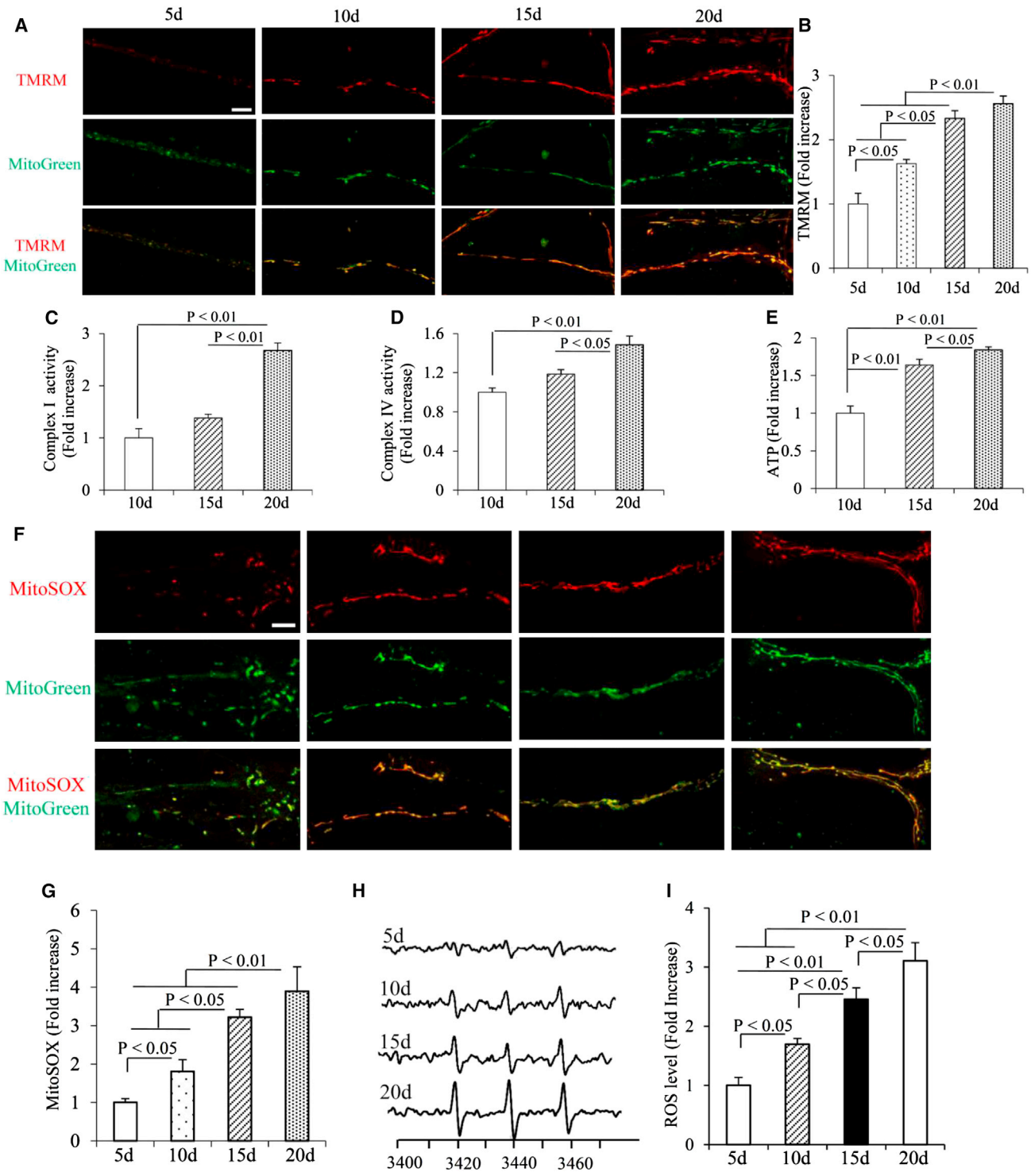

Figure 3. Development of Mitochondrial Functions in hiPSC-Derived DA Neurons

(A–G) Mitochondrial membrane potential and ROS levels were measured by TMRM (A and B). Representative images for TMRM staining for hiPSC-derived DA neurons cultured in differentiation media for 5, 10, 15, and 20 days are shown in (A), and quantifications of immunofluorescent intensity for TMRM in (B) (n = 3 independent experiments; mean ± SEM, with 5 cells quantified per experiment). Enzymatic activity of complex I (C), IV (D), and cellular ATP levels (E) were determined in cell lysates from hiPSC-derived DA neurons cultured in differentiation media for 10, 15, and 20 days (n = 3 independent experiments; mean ± SEM in C–E). Mitochondrial ROS levels were

(legend continued on next page)

These data suggest that upregulation of ROS production may be important for maintaining mitochondrial homeostasis, contributing to DA neuron differentiation and maturation.

Alterations in Mitochondrial Morphology and Mobility in hiPSC Differentiated DA Neurons

Next, we compared mitochondrial morphology and mobility in the processes of hiPSC differentiated to DA neurons. Using MitoGreen staining (Figures 3A and 3F) as a mitochondrial marker, we observed that mitochondria in day-5 and day-10 DA neurons were mostly short in length and dot shaped, whereas mitochondria became longer on later differential days. Increased densities of both short and long mitochondria were detected as the differentiation process continued. Compared with day-5 neurons, mitochondrial density increased by 1.4- and 2.0-fold in each process (100 μm in length) in DA neurons differentiated for 15 and 20 days, respectively (Figure 4A). The number of mitochondria in all processes of each neuron was increased by 2.2- and 5.9-fold on days 15 and 20, respectively (Figure 4B). The average length of mitochondria was 2.1 μm, 3.2 μm, and 3.8 μm on days 10, 15, and 20, respectively (Figure 4C). Most mitochondria were shorter than 2 μm or ranged from 2 to 4 μm on day 10. In contrast, day-15 and day-20 mitochondria were longer than 4 μm or ranged from 2 to 4 μm. Fewer than 3% of day-20 mitochondria were shorter than 2 μm (Figure 4D). Cumulative distribution data clearly demonstrated accumulated percentile of long mitochondria over time under differentiation induction (Figure 4E).

We further investigated dynamic indicators of mitochondria movement. Compared with the mitochondria from the day-10 differentiated DA neurons (Movie S1A), mitochondria were elongated and displayed higher movement speed with significantly longer travel distance in neuronal processes of hiPSC-derived DA neurons differentiated for 15 (Movie S1B) and 20 days (Movie S1C). Mitochondrial travel distance (Figure 4F), velocity (Figure 4G), and the percentage of anterograde and retrograde movable mitochondria (Figures 4H and 4I) increased, while the percentage of stationary mitochondria decreased over the time course of differentiation and maturation (Figure 4H). Representative kymograph images (Figure 4J) showed more movable mitochondria in the processes of the day-15 and -20 differentiated DA neurons. Collectively, our results demonstrate increased dynamics in mitochondria of hiPSC-derived DA neurons during differentiation.

Effect of Mitochondrial Function on DA Neuron-Directed Differentiation

To investigate the effect of mitochondrial respiratory function on DA neuron differentiation, we blocked key enzyme activity in the respiratory chain by incubation of potassium cyanide (KCN), a complex IV inhibitor (500 nM), and rotenone, a complex I inhibitor (10 nM) with cells, respectively, and then analyzed the differentiation ability of DA neurons. As shown in Figure 5A, the inhibitors/toxins for mitochondrial respiratory chains were added 2 days after the rosettes were plated. Earlier applications of the inhibitors to the stage of undifferentiated hiPCS (Figure S2A) resulted in significantly smaller-sized EBs (Figures S2B and S2C), disabilities in rosette formation (Figures S2D–S2G), and significant reduction in complex IV and I activities (Figures S2H and S2I), and ATP levels (Figure S2J).

We next measured the TUJ1- or TH-positive process length in day-20 differentiated neurons. Both indicators were markedly decreased with KCN and rotenone treatments (Figures 5B and 5C). Similarly, the number of SYN-positive puncta (Figures 5D and 5E) and its protein levels were significantly reduced in day-20 DA neurons with the treatment of mitochondrial inhibitors (Figure 5F). These data indicate that mitochondrial dysfunction inhibits DA neuron maturation and synaptogenesis in our differentiation system.

To further validate the midbrain dopaminergic neurons, we quantified levels of earlier markers for DA neuronal maturation by real-time PCR. In comparison with vehicle-treated mitochondria, not only were the levels of earlier markers, such as *EN1*, *FOXA2*, *LMX1A*, and *OTX2*, significantly lower in DA neurons under KCN and rotenone treatments (Figures 5G–5J), but also their decreasing rates were relatively slow over the induction time.

measured by MitoSOX staining (F and G). Representative images for MitoSOX staining for hiPSC-derived DA neurons cultured in differentiation media for 5, 10, 15, and 20 days are shown in (F). Quantification of immunofluorescent intensity for MitoSOX is shown in (G) (n = 3 independent experiments; mean ± SEM, with five cells quantified per experiment).

(H and I) EPR for measurement of intracellular ROS levels. Representative EPR images for hiPSC-derived DA neurons cultured in differentiation media for 5, 10, 15, and 20 days are shown in (H), and quantification of EPR signals in (I) (n = 3 independent experiments; mean ± SEM).

Data are expressed as fold increase relative to DA neurons cultured in differentiation media for 10 days. Statistical analysis was performed using StatView version 5.0.1. For (B–E), (G), and (I), one-way ANOVA was used for repeated-measures analysis, followed by Fisher's protected least significant difference for post hoc comparisons. Data are presented as mean ± SEM. Three independent experiments in (A–I); n = 5 per group per experiment in (B) and (G). Scale bars in (A) and (F) represent 5 μm.

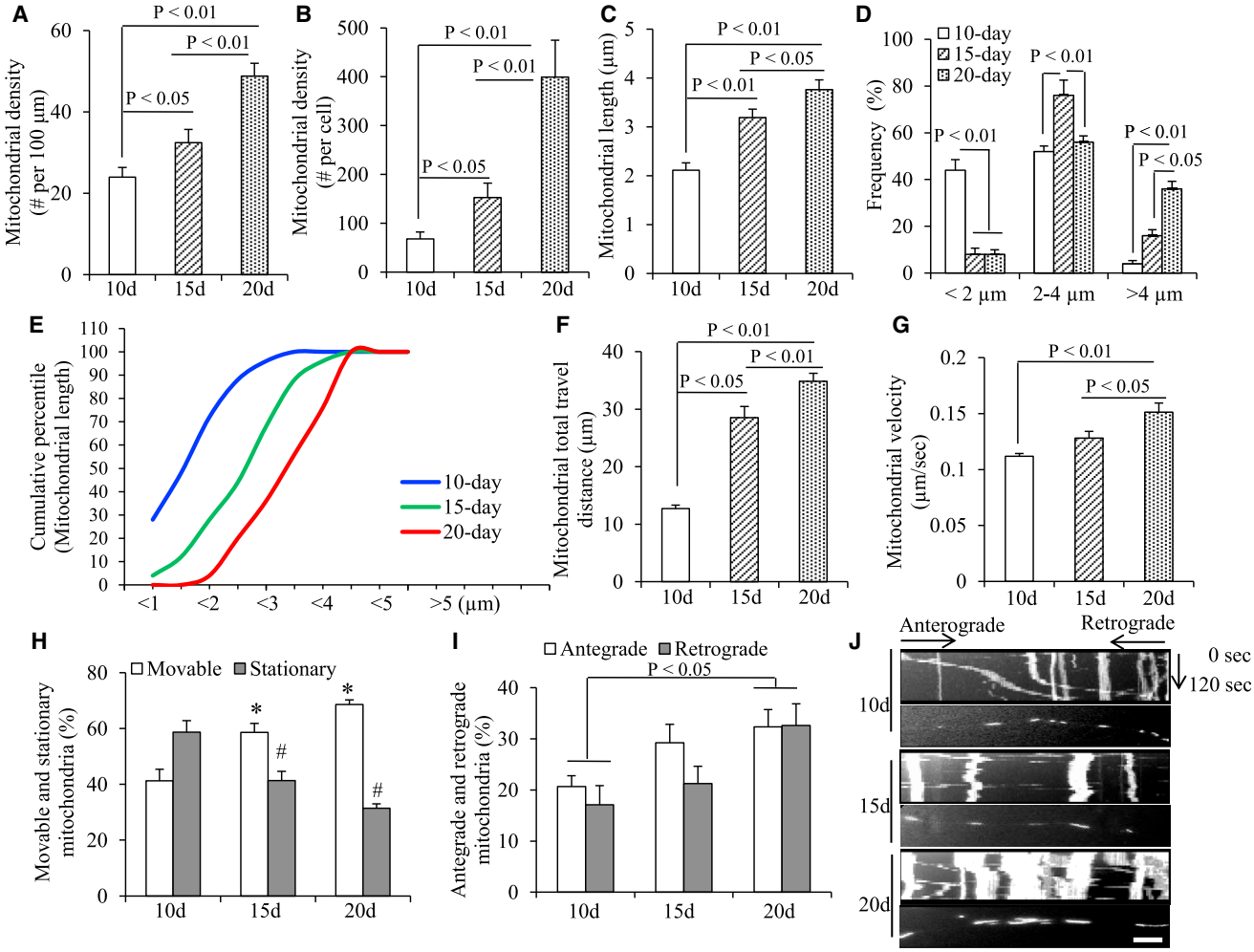

Figure 4. Development of Mitochondrial Morphological and Dynamic Parameters in hiPSC-Derived DA Neurons

(A–D) Morphological changes in mitochondria of hiPSC-derived DA neurons cultured in differentiation media for 10, 15, and 20 days were measured and compared. Average mitochondrial density (in each 100-μm process in A and in all processes of each DA neuron in B), length (C), and frequency (D) in the processes of DA neurons were quantified.

(E) Cumulative distribution data showed increases in the numbers of long mitochondria and decreases in fragmentation of small mitochondria at 10, 15, and 20 days after differentiation induction (n = 3 independent experiments; mean ± SEM, with 10 mitochondria quantified per experiment in A–E).

(F–I) Average mitochondrial travel distance (F) and mitochondrial travel velocity (G) were calculated. The percentage of stationary (H), anterograde, and retrograde movable mitochondria (I) in DA neurons differentiated for varying days was compared. (n = 3 independent experiments; mean ± SEM, with 10 mitochondrial movements quantified per experiment in F–I).

(J) Kymographs generated from live imaging movies represent hiPSC-derived DA neurons cultured in differentiation media for 10, 15, and 20 days. In the kymographs, the x axis is mitochondrial position and the y axis represents the time lapse of 0–120 s. Vertical white lines represent stationary mitochondria and diagonal lines represent moving mitochondria. Anterograde movements are from left to right and retrograde movements are from right to left.

*$p < 0.05$ versus day-10 movable mitochondria and $^{\#}p < 0.05$ versus day-10 stationary mitochondria in (H). Scale bar, 10 μm in (J). Statistical analysis was performed using StatView version 5.0.1. For (A–D) and (F–I), one-way ANOVA was used for repeated-measures analysis, followed by Fisher's protected least significant difference for post hoc comparisons. Data are presented as mean ± SEM. Three independent experiments in (A–I); n = 10 per group per experiment in (A–I).

Similarly, the expression levels for mature DA neurons including *AADC*, *DAT*, *VMAT2*, and mature neurons, *MAP2*, were completely blocked in the presence of KCN and rotenone (Figures 5K–5N). These results demonstrate a direct link between mitochondrial alteration and DA neuron differentiation and maturation.

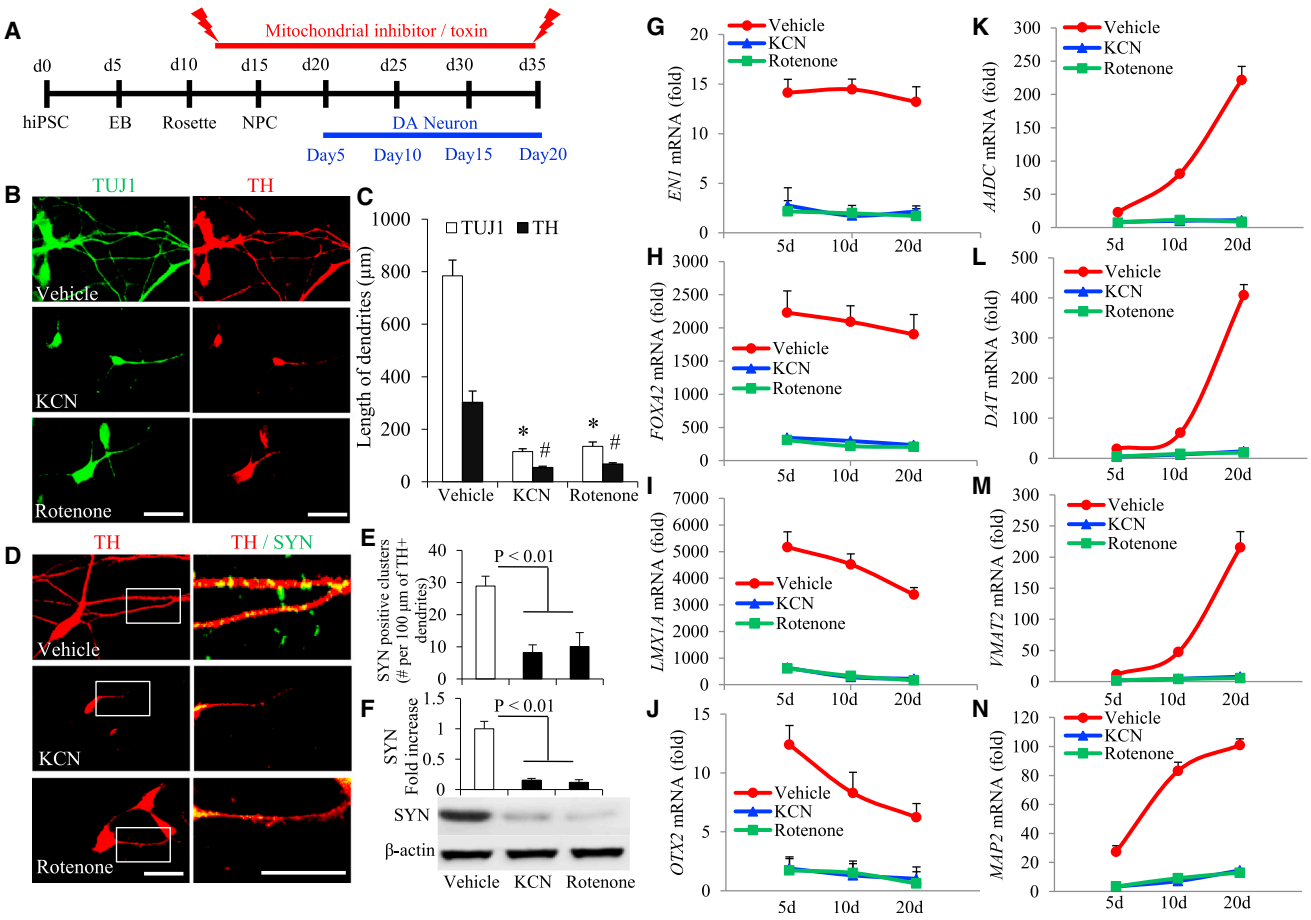

Figure 5. Effect of Mitochondrial Inhibitor KCN or Rotenone on Differentiation of hiPSC Line-Induced Human DA Neurons

(A) Schematic representation of differentiation of hiPSC line-induced DA neurons under KCN or rotenone treatment.

(B and C) Co-expression of TUJ1 and TH in hiPSC-induced neurons cultured in differentiation media for 20 days under KCN or rotenone treatment. (B) Representative images for immunostaining of TUJ1 (green) and TH (red). Scale bars, 50 μm. (C) Quantification of neuronal process length of TUJ1-positive neurons and TH-positive DA neurons in differentiation media for different days was performed using NIH ImageJ. $^{\#}p < 0.01$ compared with vehicle (day-20) cells, length of TUJ1 positive dendrites, and $^{*}p < 0.01$ compared with vehicle (day-20) cells, length of TH positive dendrites (n = 3 independent experiments; mean ± SEM, with 10 cells quantified per experiment).

(D) Immunocytochemistry of SYN (green) and TH (red). Scale bars, 50 μm.

(E) Quantification of numbers of SYN-positive clusters along the branches of hiPSC-derived DA neurons cultured in differentiation media for 20 days with or without KCN or rotenone treatment (n = 3 independent experiments; mean ± SEM, with 10 cells quantified per experiment).

(F) Immunoblotting for SYN protein expression. Quantification of SYN expression level is shown in the upper panel. Data are normalized to the expression level of internal control β-actin. Representative images are shown for SYN and β-actin in the lower panel (n = 3 independent experiments; mean ± SEM).

(G–N) Real-time qPCR results for gene expression. The expression level of the undifferentiated hiPSC cells was set to 1 (n = 3 independent experiments; mean ± SEM).

Statistical analysis was performed using StatView version 5.0.1. For (C), (E), and (F), one-way ANOVA was used for repeated-measures analysis, followed by Fisher's protected least significant difference for post hoc comparisons. Data are presented as mean ± SEM. Three independent experiments in (B–N); n = 10 per group per experiment in (C) and (E).

Effect of Mitochondrial Function on the Development of Mitochondrial Functions, Morphology, and Mobility in hiPSC-Derived DA Neurons

We then assessed the effects of mitochondrial inhibitors on mitochondrial membrane potential and ROS levels. TMRM staining, an indicator for membrane potential, was reduced by ~66% (Figures 6A and 6B). Mitochondrial superoxide, as shown by MitoSOX staining, was increased by ~2.2-fold in KCN and rotenone-treated day-20 DA neurons, respectively (Figures 6C and 6D), which was consistent with the

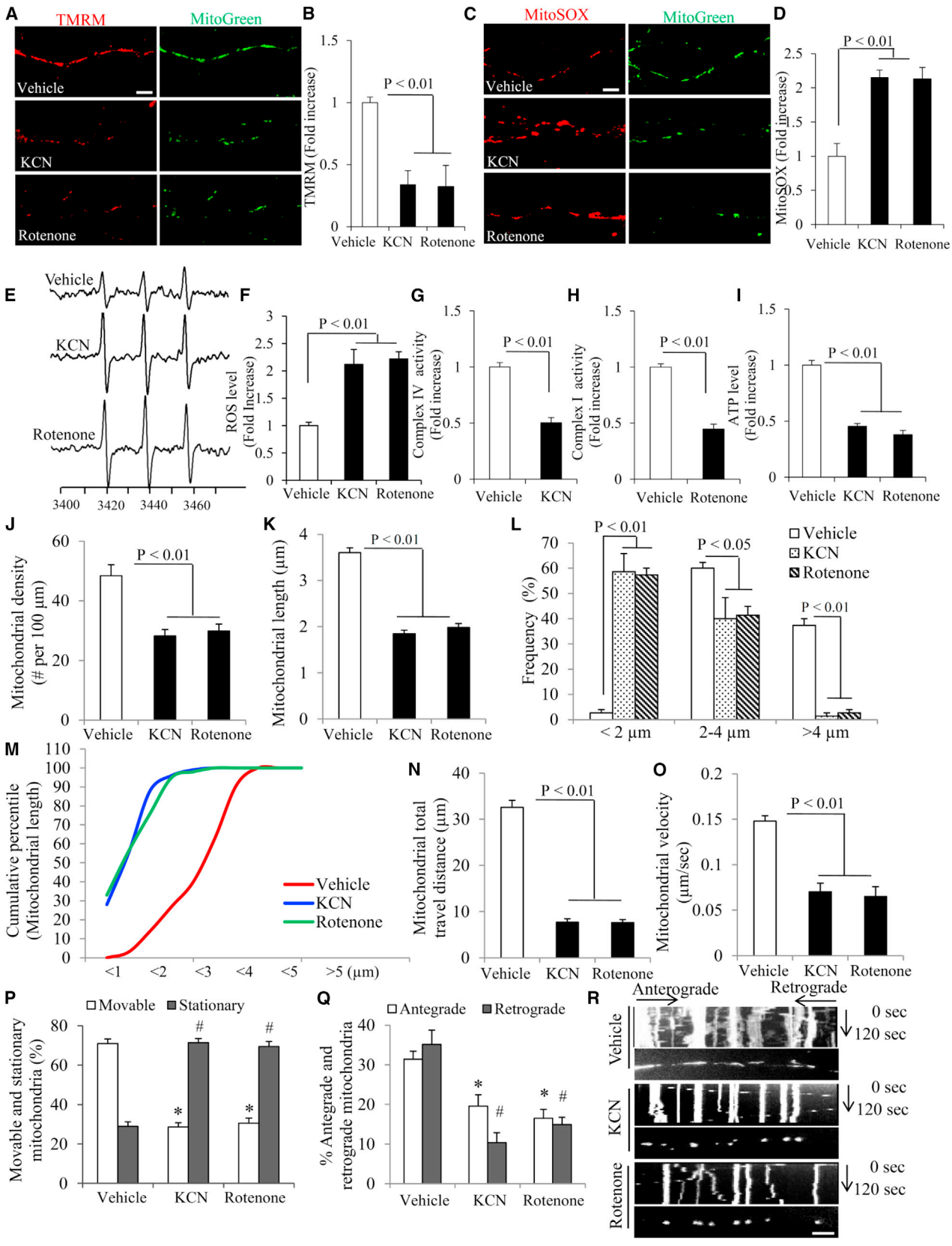

(legend on next page)

EPR results showing a significant increase in ROS levels in cells treated with KCN or rotenone (Figures 6E and 6F). Accordingly, treatment of KCN or rotenone suppressed the activity of complex IV (Figure 6G) and I (Figure 6H), and ATP levels (Figure 6I) in day-20 neurons. To determine the effect of mitochondrial inhibitor/toxins on mitochondria morphological changes in day-20 DA neurons, we stained cells with MitoGreen to visualize mitochondrial morphology (Figures 6A and 6C). Compared with vehicle-treated day-20 DA neurons, KCN or rotenone treatment resulted in a decrease in mitochondrial density and length with mostly shorter and dot-shaped mitochondria (Figures 6J–6L). The percentage of short mitochondria was significantly elevated over time under KCN and rotenone treatments (Figure 6M).

We further investigated dynamic changes in mitochondria movement. Compared with the mitochondria from the day-20 differentiated DA neurons treated with vehicle (Movie S1D), mitochondria in neuronal processes of DA neurons with KCN (Movie S1E) and rotenone treatments (Movie S1F) displayed less movable and more stationary mitochondria. Similarly, treatment with KCN or rotenone significantly reduced mitochondrial travel distance (Figure 6N), velocity (Figure 6O), and the percentage of anterograde and retrograde movable mitochondria (Figures 6P and 6Q). Conversely, the percentage of stationary mitochondria was increased in cells treated with KCN or rotenone (Figure 6P). Representative kymograph images (Figure 6R) showed less movable mitochondria in the processes of the day-20 differentiated DA neurons with KCN and rotenone treatments. These data demonstrate that aberrant mitochondrial function significantly reduces mitochondrial dynamics in hiPSC-derived DA neurons.

DISCUSSION

A recent study suggested that mitochondrial dysfunction occurs in patient-derived hiPSC-induced human neurons (Cooper et al., 2012), but detailed investigation of such mitochondrial dysfunction in hiPSC-derived DA neurons has yet to be undertaken. In this study, we comprehensively monitored the differentiation, synaptogenesis, and development of mitochondrial functions of hiPSC-induced human DA neurons by examining neurophysiology and mitochondrial and synaptic function and structure. Our results obtained from neurophysiology reveal increases in resting membrane potential, action potential, and conductance of voltage-gated Na^+ channels and K^+ channels in a time-dependent manner in hiPSC-derived DA neurons under our differentiation protocol. These data are indicative of membrane maturation over time in differentiating

Figure 6. Effect of Mitochondrial Toxin KCN or Rotenone on Development of Mitochondrial Functional, Morphological, and Dynamic Parameters in hiPSC-Derived DA Neurons

(A–D) Mitochondrial membrane potential and ROS levels were measured by TMRM (A and B) and MitoSOX staining (C and D), respectively. Representative images for TMRM and MitoSOX staining for hiPSC-derived DA neurons cultured in differentiation media for 20 days with or without KCN or rotenone treatment are shown in (A) and (C), and quantifications of immunofluorescent intensity in (B) and (D) (n = 3 independent experiments; mean ± SEM, with five cells quantified per experiment in A–D). Scale bars, 5 μm.

(E and F) Assessment of intracellular ROS levels measured by EPR spectroscopy. Representative images for EPR are shown in (E) and quantifications in (F) (n = 3 independent experiments; mean ± SEM).

(G–I) Activities of complex IV (G) and I (H), and ATP levels (I) were determined in hiPSC-derived DA neurons cultured in differentiation media for 20 days with above treatments. Data are expressed as fold increase relative to vehicle DA neurons cultured in differentiation media for 20 days (n = 3 independent experiments; mean ± SEM).

(J–Q) Morphological changes in mitochondria of hiPSC-derived DA neurons cultured in differentiation media for 20 days with or without KCN or rotenone treatment. Average mitochondrial density (J), length (K), and frequency (L) in the processes of DA neurons were quantified. (M) Cumulative distribution data showed decreases in the numbers of long mitochondria and increases in fragmentation of small mitochondria with KCN or rotenone treatment (n = 3 independent experiments; mean ± SEM, with 10 mitochondria quantified per experiment in J–M). Average mitochondrial travel distance (N) and mitochondrial travel velocity (O) were calculated. The percentage of stationary (P), anterograde, and retrograde movable mitochondria (Q) in DA neurons differentiated for varying days was compared (n = 3 independent experiments; mean ± SEM, with 10 mitochondrial movements quantified per experiment in (N–Q).

(R) Kymographs generated from live imaging movies represent hiPSC-derived DA neurons cultured in differentiation media for 20 days with or without KCN or rotenone treatment. In the kymographs, the x axis is mitochondrial position and the y axis represents the time lapse of 0–120 s. Vertical white lines represent stationary mitochondria and diagonal lines represent moving mitochondria. Anterograde movements are from left to right and retrograde movements are from right to left.

*$p < 0.05$ versus vehicle (day-20) movable mitochondria and $^{\#}p < 0.05$ versus vehicle (day-20) stationary mitochondria in (P and Q). Scale bar, 10 μm in (R). Statistical analysis was performed using StatView version 5.0.1. For (B), (D), (F), (I–L), and (N–Q), one-way ANOVA was used for repeated-measures analysis, followed by Fisher's protected least significant difference for post hoc comparisons. For (G) and (H), Student's t test was used for repeated-measures analysis. Data are presented as mean ± SEM. Three independent experiments in (A–R); n = 5 cells per group per experiment in (B) and (D), and n = 10 mitochondrial movements per group per experiment in (J–Q).

neuronal cells starting at day 15 after treatment with DA differential media and peaking at day 20 in our present study. Consistent with the alterations in neurophysiologic properties, neuronal process length and expression levels of both neuronal protein markers, TUJ1 and TH (a dopaminergic neuronal marker), were altered in a similar pattern. In addition, earlier markers, the transcription factors expressed in midbrain dopaminergic neuron progenitors or immature dopaminergic neurons, including *LMX1A* (Andersson et al., 2006), *EN1* (Simon et al., 2001), *FOXA2* (Nakatani et al., 2010), and *OTX2* (Millet et al., 1996), all reached a plateau at the NPCs stage, while levels of markers for mature DA neurons including *DAT*, *AADC*, and *VMAT2* (Ang, 2006; Bjorklund et al., 2002; Kim et al., 2011), as well as the marker for mature neurons, *MAP2*, all increased during the course of dopaminergic neuron induction. These results suggest, starting from the NPCs stage, continuous maturation of hiPSC-derived DA neurons over time with maximal adult values achieved by 20 days after induction with DA neuronal media.

During development, neurons assemble to form cultivated neuronal networks. One of the critical indicators of neural network formation is synaptogenesis (Colon-Ramos, 2009). We observed increased synaptophysin expression levels and number of synaptophysin-positive puncta over time. Moreover, we noted spontaneous postsynaptic current generation starting at day 15 after treatment with DA differential media, suggesting the capacity to form functional synapses. Consistent with prior studies of directed differentiation to functional neuronal networks (Hartfield et al., 2014; Yang et al., 2008), a critical step in our protocol for EB induction involves switching to media with neural induction medium (NIM) the day after EB formed, to promote neuronal differentiation. Given the beneficial role of Sonic Hedgehog (SHH) signaling in the control of dorsal midbrain development (Martinez et al., 2013), we added SHH to the DA expansion medium to govern the formation of DA neurons.

ROS are a double-edged sword in biological systems, as they can be either beneficial to living systems during oxygen-dependent reactions and aerobic respiration or harmful if overproduced (Sena and Chandel, 2012). We demonstrated that ROS levels were increased during hiPSC-derived DA neuron differentiation and maturation, suggesting that increased ROS levels serve as an important stimulus associated with neuronal development. Accordingly, mitochondrial membrane potential, as an indicator of mitochondrial function, also increased over time. In addition, increased ROS levels and membrane potential were in line with increases in key enzyme activity associated with the respiratory chains, including complex I and IV activity, and ATP levels. Thus, mitochondrial function is enhanced during the course of DA neuron differentiation from hiPSCs. As by-products of oxidative phosphorylation, the production of large amounts of ATP through the mitochondrial electron transport chain is associated with ROS generation and accumulation. Similarly, ATP and ROS levels were increased in differentiated cells from hESCs after 14 days of differentiation (Cho et al., 2006). The increased levels of ROS were accompanied by upregulation of ATP levels.

Consistent with results showing increased mitochondrial function, mitochondrial morphology and distribution were altered during differentiation. Mitochondrial density was increased significantly both in neuronal processes and the whole cell. Mitochondria become elongated during the maturation of cells differentiated from hESCs and hiPSCs (Cho et al., 2006; St John et al., 2005; Varum et al., 2011). Furthermore, mitochondrial movement and transport also increased during differentiation, as shown by trends in mitochondrial travel distance, velocity, and percentage of both retrograde and anterograde movable mitochondria. These results suggest increased mitochondrial dynamics during DA neuronal development.

The essential role of mitochondria in the differentiation of DA neurons was further confirmed by application of mitochondrial inhibitors/toxins to suppress respiratory chain complexes IV and I from the NPCs stages. Treatment with KCN or rotenone significantly inhibited the differentiation and maturation of DA neurons along with alterations in mitochondrial structure and function. In addition, significantly lower levels of transcription factors in progenitor, immature, and mature DA neurons were detected with KCN and rotenone treatments at different differentiation stages, indicating that the poor development of DA neurons induced by mitochondrial malfunctions could also have resulted from interference with the expression of transcription factors for DA neurons. Interestingly, at the hiPSCs stage, application of KCN and rotenone inhibited the formation of EBs and rosettes (Figure 2), which ultimately resulted in failure of induction of DA neurons. These results further uncover the importance of mitochondrial function in DA neuronal development, not only in the maturation of NPCs and immature DA neurons but also in the early stages before NPC generation.

During differentiation, mitochondrial maturation requires a dynamic network and a continuous balance between fission and fusion processes. The balance is maintained via quality control of mitochondrial fission and fusion proteins. Drp1 (Yoon et al., 2003), a key mitochondria protein controlling fission and biogenesis, has recently been found to be indispensable in somatic cell reprogramming to pluripotency (Vazquez-Martin et al., 2012) as well as in differentiation of ESCs (Wang et al., 2014). However,

further investigation is required to determine whether Drp1 is involved in neurogenesis from iPSCs, and whether the mitochondrial proteins controlling fusion events, such as fusion proteins mitofusin 2 and optic atrophy 1 (Chen et al., 2003), and mitochondrial trafficking regulator Miro1 (mitochondrial rho GTPase 1) (Birsa et al., 2013), key factors in normal embryonic development (Chen et al., 2003; Yamaoka et al., 2011; Yoon et al., 2003), are also involved in the differentiation and maturation of iPSCs.

In summary, we have provided direct evidence of the involvement of mitochondrial development in DA neuron differentiation and maturation, and also provided a neurophysiologic model of mitochondrial development during neurogenesis of DA neurons. We comprehensively evaluated the properties of neuronal and mitochondrial structure and function during the course of formation and maturation of human DA neurons derived from hiPSCs. Our data clearly demonstrated the direct role of mitochondria in DA neuron maturation. The present model provides an approach for the study of abnormal mitochondrial structure, function, and dynamics in the pathogenesis of neurodegenerative diseases such as PD.

EXPERIMENTAL PROCEDURES

hiPSC Culture

BM2-3 hiPSCs from passages 16 to 20 were obtained from Dr. Sunita L. D'Souza. This BM2-3 iPSC line was derived from bone marrow of a human subject clinically normal and verified by fluorescent in situ hybridization test showing 46,XY. Cytogenetic analysis of cultured human stem cells revealed a normal female karyotype. This analysis does not show any evidence of a clinically significant numerical or structural chromosome abnormality. Cells were maintained under feeder-free conditions using Matrigel (BD Biosciences)-coated 6-well tissue culture plates in Essential 8 Medium (E8, Life Technologies), supplemented with 10 μM ROCK inhibitor Y27632 (Life Technologies) on passaging days. Cells were routinely passaged as small clumps using a previously described EDTA method (Beers et al., 2012).

Formation of Embryoid Bodies and Induction of Rosette

Feeder-free iPSCs were dissociated with TryplE and seeded onto AggreWell800 plate (10,000 cells per EB; Stem Cell Technologies) in E8 medium supplemented with 10 μM ROCK inhibitor Y27632 for the first 24 hr; we changed 75% of the medium daily with STEMdiff NIM (Stem Cell Technologies). EBs were harvested after 5 days and plated onto poly-L-ornithine/laminin (PLO/L, Sigma)-coated plates. One to two days after attachment, prominent neural rosette structures were visible inside the attached neural aggregates. EBs were traced with ImageJ software. Rosettes were formed by cells expressing proteins characteristic of progenitor markers of PAX6 and Ki67.

Isolation of Stem/Progenitor Cells and Differentiation of DA Neurons

We followed the differentiation protocol of Hartfield et al. (2014) with some modifications. In brief, stem/progenitor cells from neuronal rosette clusters were isolated using Neural Rosette Selection Reagent (Stem Cell Technologies) 5 days after incubation in NIM. Detached cells were collected and plated onto PLO/L-coated 6-well plates for western blot analysis and complex activities measurement (2×10^4 cells per well), 12-well plates for co-culture system (1×10^4 cells per well), or coverslips for immunocytochemistry and electrophysiology (5×10^3 cells per coverslip). NPCs were cultured in neural expansion medium (DMEM/F12 supplemented with 1× B27 and N2 [Life Technologies], fibroblast growth factor 8a [100 ng/mL, Life Technologies], SHH C25II [200 ng/mL, Life Technologies], heparin [2 μg/mL, Life Technologies], and 1× non-essential amino acids [Life Technologies]) for 5 days and finally in DA neuronal differentiation medium (neurobasal medium supplemented with L-glutamine [2 mM, Life Technologies], 1× B27 and N2 supplements, brain-derived neurotrophic factor [25 ng/mL], glial-derived neurotrophic factor [20 ng/mL], N6,29-O-dibutyryladenosine 39,59-cyclic monophosphate sodium salt [100 μM, Sigma], and ascorbic acid [200 μM, Sigma]) for 5, 10, 15, and 20 days before further analysis.

For investigating the effects of KCN and Rotenone on DA neuronal induction or rosette formation, a final concentration of 500 nM KCN or 10 nM rotenone was added into the cultural medium at 2 days after rosette induction (Figure 5A), or hiPSCs (Figure S2) and KCN and rotenone were added during each medium change afterward.

SUPPLEMENTAL INFORMATION

Supplemental Information includes Supplemental Experimental Procedures, two figures, and one movie and can be found with this article online at http://dx.doi.org/10.1016/j.stemcr.2016.08.014.

AUTHOR CONTRIBUTIONS

S.S.Y. directed, designed, and supervised research, and wrote the manuscript. D.F., Q.Y., and D.C. conducted experiments, analyzed data, and wrote the manuscript. S.Y. performed electrophysiology experiments and analyzed data.

ACKNOWLEDGMENTS

We thank Dr. Sunita L. D'Souza (Department of Gene and Cell Medicine and Black Family Stem Cell Institute, Mount Sinai School of Medicine, New York, NY, USA; and Department of Developmental and Regenerative Biology, Icahn School of Medicine at Mount Sinai, New York, NY, USA) for providing iPSCs for the study. This study was supported by grants from the National Institute on Aging (R37AG037319 and R01AG044793) and the National Institute of Neurological Disorder and Stroke (R01NS089116).

Received: September 15, 2015
Revised: August 22, 2016
Accepted: August 23, 2016
Published: September 22, 2016

REFERENCES

Andersson, E., Tryggvason, U., Deng, Q., Friling, S., Alekseenko, Z., Robert, B., Perlmann, T., and Ericson, J. (2006). Identification of intrinsic determinants of midbrain dopamine neurons. Cell *124*, 393–405.

Ang, S.L. (2006). Transcriptional control of midbrain dopaminergic neuron development. Development *133*, 3499–3506.

Armstrong, L., Tilgner, K., Saretzki, G., Atkinson, S.P., Stojkovic, M., Moreno, R., Przyborski, S., and Lako, M. (2010). Human induced pluripotent stem cell lines show stress defense mechanisms and mitochondrial regulation similar to those of human embryonic stem cells. Stem Cells *28*, 661–673.

Asensi, K.D., Fortunato, R.S., dos Santos, D.S., Pacheco, T.S., de Rezende, D.F., Rodrigues, D.C., Mesquita, F.C., Kasai-Brunswick, T.H., de Carvalho, A.C., Carvalho, D.P., et al. (2014). Reprogramming to a pluripotent state modifies mesenchymal stem cell resistance to oxidative stress. J. Cell Mol. Med. *18*, 824–831.

Beers, J., Gulbranson, D.R., George, N., Siniscalchi, L.I., Jones, J., Thomson, J.A., and Chen, G. (2012). Passaging and colony expansion of human pluripotent stem cells by enzyme-free dissociation in chemically defined culture conditions. Nat. Protoc. *7*, 2029–2040.

Birsa, N., Norkett, R., Higgs, N., Lopez-Domenech, G., and Kittler, J.T. (2013). Mitochondrial trafficking in neurons and the role of the Miro family of GTPase proteins. Biochem. Soc. Trans. *41*, 1525–1531.

Bjorklund, L.M., Sanchez-Pernaute, R., Chung, S., Andersson, T., Chen, I.Y., McNaught, K.S., Brownell, A.L., Jenkins, B.G., Wahlestedt, C., Kim, K.S., et al. (2002). Embryonic stem cells develop into functional dopaminergic neurons after transplantation in a Parkinson rat model. Proc. Natl. Acad. Sci. USA *99*, 2344–2349.

Bukowiecki, R., Adjaye, J., and Prigione, A. (2014). Mitochondrial function in pluripotent stem cells and cellular reprogramming. Gerontology *60*, 174–182.

Chandel, N.S., Maltepe, E., Goldwasser, E., Mathieu, C.E., Simon, M.C., and Schumacker, P.T. (1998). Mitochondrial reactive oxygen species trigger hypoxia-induced transcription. Proc. Natl. Acad. Sci. USA *95*, 11715–11720.

Chen, H., Detmer, S.A., Ewald, A.J., Griffin, E.E., Fraser, S.E., and Chan, D.C. (2003). Mitofusins Mfn1 and Mfn2 coordinately regulate mitochondrial fusion and are essential for embryonic development. J. Cell Biol. *160*, 189–200.

Cho, Y.M., Kwon, S., Pak, Y.K., Seol, H.W., Choi, Y.M., Park do, J., Park, K.S., and Lee, H.K. (2006). Dynamic changes in mitochondrial biogenesis and antioxidant enzymes during the spontaneous differentiation of human embryonic stem cells. Biochem. Biophys. Res. Commun. *348*, 1472–1478.

Colon-Ramos, D.A. (2009). Synapse formation in developing neural circuits. Curr. Top. Dev. Biol. *87*, 53–79.

Cooper, O., Seo, H., Andrabi, S., Guardia-Laguarta, C., Graziotto, J., Sundberg, M., McLean, J.R., Carrillo-Reid, L., Xie, Z., Osborn, T., et al. (2012). Pharmacological rescue of mitochondrial deficits in iPSC-derived neural cells from patients with familial Parkinson's disease. Sci. Transl. Med. *4*, 141ra190.

Genova, M.L., Pich, M.M., Bernacchia, A., Bianchi, C., Biondi, A., Bovina, C., Falasca, A.I., Formiggini, G., Castelli, G.P., and Lenaz, G. (2004). The mitochondrial production of reactive oxygen species in relation to aging and pathology. Ann. N. Y. Acad. Sci. *1011*, 86–100.

Hartfield, E.M., Yamasaki-Mann, M., Ribeiro Fernandes, H.J., Vowles, J., James, W.S., Cowley, S.A., and Wade-Martins, R. (2014). Physiological characterisation of human iPS-derived dopaminergic neurons. PLoS One *9*, e87388.

Kim, J., Su, S.C., Wang, H., Cheng, A.W., Cassady, J.P., Lodato, M.A., Lengner, C.J., Chung, C.Y., Dawlaty, M.M., Tsai, L.H., et al. (2011). Functional integration of dopaminergic neurons directly converted from mouse fibroblasts. Cell Stem Cell *9*, 413–419.

Martinez, C., Cornejo, V.H., Lois, P., Ellis, T., Solis, N.P., Wainwright, B.J., and Palma, V. (2013). Proliferation of murine midbrain neural stem cells depends upon an endogenous sonic hedgehog (Shh) source. PLoS One *8*, e65818.

Mattson, M.P., Gleichmann, M., and Cheng, A. (2008). Mitochondria in neuroplasticity and neurological disorders. Neuron *60*, 748–766.

Millet, S., Bloch-Gallego, E., Simeone, A., and Alvarado-Mallart, R.M. (1996). The caudal limit of Otx2 gene expression as a marker of the midbrain/hindbrain boundary: a study using in situ hybridisation and chick/quail homotopic grafts. Development *122*, 3785–3797.

Nakatani, T., Kumai, M., Mizuhara, E., Minaki, Y., and Ono, Y. (2010). Lmx1a and Lmx1b cooperate with Foxa2 to coordinate the specification of dopaminergic neurons and control of floor plate cell differentiation in the developing mesencephalon. Dev. Biol. *339*, 101–113.

O'Brien, L.C., Keeney, P.M., and Bennett, J.P., Jr. (2015). Differentiation of human neural stem cells into motor neurons stimulates mitochondrial biogenesis and decreases glycolytic flux. Stem Cells Dev. *24*, 1984–1994.

Perier, C., and Vila, M. (2012). Mitochondrial biology and Parkinson's disease. Cold Spring Harbor Perspect. Med. *2*, a009332.

Prigione, A., Lichtner, B., Kuhl, H., Struys, E.A., Wamelink, M., Lehrach, H., Ralser, M., Timmermann, B., and Adjaye, J. (2011). Human induced pluripotent stem cells harbor homoplasmic and heteroplasmic mitochondrial DNA mutations while maintaining human embryonic stem cell-like metabolic reprogramming. Stem Cells *29*, 1338–1348.

Sena, L.A., and Chandel, N.S. (2012). Physiological roles of mitochondrial reactive oxygen species. Mol. Cell *48*, 158–167.

Simon, H.H., Saueressig, H., Wurst, W., Goulding, M.D., and O'Leary, D.D. (2001). Fate of midbrain dopaminergic neurons controlled by the engrailed genes. J. Neurosci. *21*, 3126–3134.

St John, J.C., Ramalho-Santos, J., Gray, H.L., Petrosko, P., Rawe, V.Y., Navara, C.S., Simerly, C.R., and Schatten, G.P. (2005). The expression of mitochondrial DNA transcription factors during early cardiomyocyte in vitro differentiation from human embryonic stem cells. Cloning Stem Cells *7*, 141–153.

Takahashi, K., and Yamanaka, S. (2006). Induction of pluripotent stem cells from mouse embryonic and adult fibroblast cultures by defined factors. Cell *126*, 663–676.

Tapia, P.C. (2006). Sublethal mitochondrial stress with an attendant stoichiometric augmentation of reactive oxygen species may precipitate many of the beneficial alterations in cellular physiology produced by caloric restriction, intermittent fasting, exercise and dietary phytonutrients: "Mitohormesis" for health and vitality. Med. Hypotheses *66*, 832–843.

Teslaa, T., and Teitell, M.A. (2015). Pluripotent stem cell energy metabolism: an update. EMBO J. *34*, 138–153.

Varum, S., Momcilovic, O., Castro, C., Ben-Yehudah, A., Ramalho-Santos, J., and Navara, C.S. (2009). Enhancement of human embryonic stem cell pluripotency through inhibition of the mitochondrial respiratory chain. Stem Cell Res. *3*, 142–156.

Varum, S., Rodrigues, A.S., Moura, M.B., Momcilovic, O., Easley, C.A.t., Ramalho-Santos, J., Van Houten, B., and Schatten, G. (2011). Energy metabolism in human pluripotent stem cells and their differentiated counterparts. PLoS One *6*, e20914.

Vazquez-Martin, A., Cufi, S., Corominas-Faja, B., Oliveras-Ferraros, C., Vellon, L., and Menendez, J.A. (2012). Mitochondrial fusion by pharmacological manipulation impedes somatic cell reprogramming to pluripotency: new insight into the role of mitophagy in cell stemness. Aging *4*, 393–401.

Wang, L., Ye, X., Zhao, Q., Zhou, Z., Dan, J., Zhu, Y., Chen, Q., and Liu, L. (2014). Drp1 is dispensable for mitochondria biogenesis in induction to pluripotency but required for differentiation of embryonic stem cells. Stem Cells Dev. *23*, 2422–2434.

Wu, Y., Zhang, X., Kang, X., Li, N., Wang, R., Hu, T., Xiang, M., Wang, X., Yuan, W., Chen, A., et al. (2013). Oxidative stress inhibits adhesion and transendothelial migration, and induces apoptosis and senescence of induced pluripotent stem cells. Clin. Exp. Pharmacol. Physiol. *40*, 626–634.

Xu, X., Duan, S., Yi, F., Ocampo, A., Liu, G.H., and Izpisua Belmonte, J.C. (2013a). Mitochondrial regulation in pluripotent stem cells. Cell Metab. *18*, 325–332.

Xu, X.L., Yi, F., Pan, H.Z., Duan, S.L., Ding, Z.C., Yuan, G.H., Qu, J., Zhang, H.C., and Liu, G.H. (2013b). Progress and prospects in stem cell therapy. Acta Pharmacol. Sin. *34*, 741–746.

Yamaoka, S., Nakajima, M., Fujimoto, M., and Tsutsumi, N. (2011). MIRO1 influences the morphology and intracellular distribution of mitochondria during embryonic cell division in *Arabidopsis*. Plant Cell Rep. *30*, 239–244.

Yang, D., Zhang, Z.J., Oldenburg, M., Ayala, M., and Zhang, S.C. (2008). Human embryonic stem cell-derived dopaminergic neurons reverse functional deficit in parkinsonian rats. Stem Cells *26*, 55–63.

Yoon, Y., Krueger, E.W., Oswald, B.J., and McNiven, M.A. (2003). The mitochondrial protein hFis1 regulates mitochondrial fission in mammalian cells through an interaction with the dynamin-like protein DLP1. Mol. Cell Biol. *23*, 5409–5420.

Stem Cell Reports, Volume *7*

Supplemental Information

Development and Dynamic Regulation of Mitochondrial Network in Human Midbrain Dopaminergic Neurons Differentiated from iPSCs

Du Fang, Yu Qing, Shijun Yan, Doris Chen, and Shirley ShiDu Yan

Supplemental Information

Development and Dynamic Regulation of Mitochondrial Network in Human Midbrain Dopaminergic Neurons Differentiated from iPSC

Du Fang[1,3], Yu Qing [1,2,3], Shijun Yan[1], Doris Chen[1], Shirley ShiDu Yan[1]*

Supplemental Figures and Legends

Supplementary Figure S1.

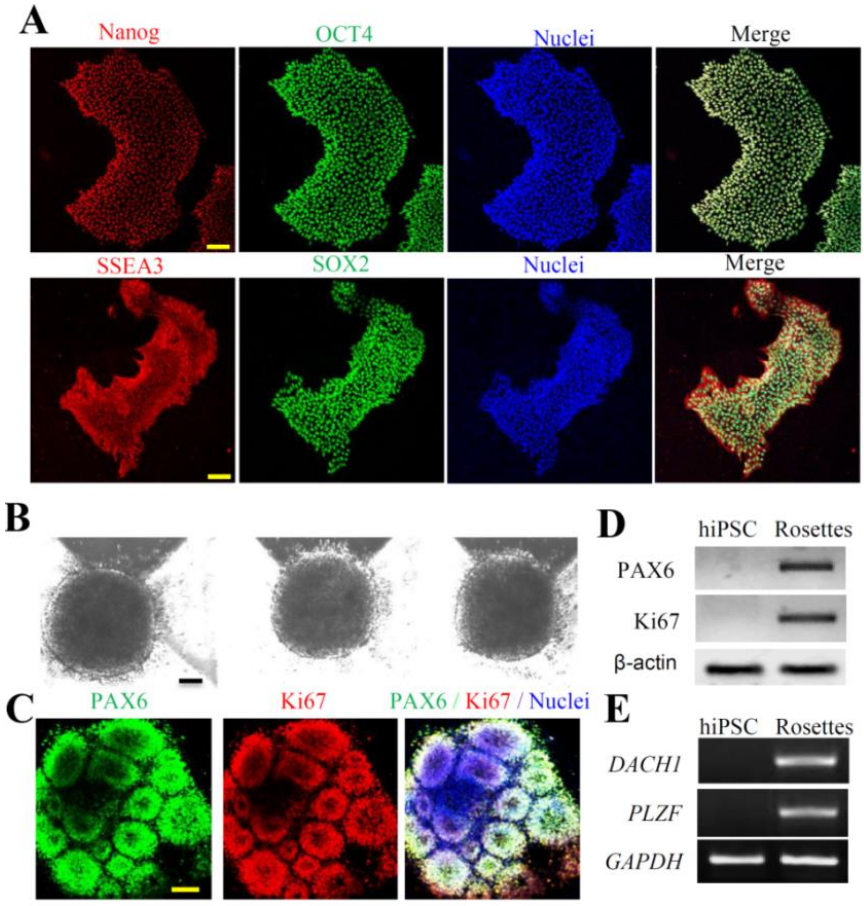

Figure S1 (Related to results: hiPSC characterization and DA neuron-directed differentiation). Characterization and identification of hiPSC line derived from normal human bone marrow fibroblasts. (S1A).

Normal human bone marrow fibroblast-derived hiPSCs BM2-3 was selected for analysis. hiPSC-BM2-3 cells expressed pluripotency markers: NANOG, OCT4, SSEA3 and SOX2. (**S1B**) Formation of embryonic bodies (EB), neural aggregates and (**S1C**) rosettes (lower panel) of hiPSC-BM2-3 cells. Images in the top panel show EB formation after forced aggregation of

hiPSC-BM2-3 cells using Aggrewells. Images in the bottom panel show rosette formations with rosette-like structures co-expressing early-stage precursor cells marker PAX6 (Green) and the mitotic marker Ki67 (Red). Nuclei were stained by DRAQ5 (5 μM, Cell Signaling), a far-red emitting fluorescent DNA dye, for 3 min at room temperature. Scale bars, 50 μm. (**S1D**) immunoblotting analysis to detect PAX6 and Ki67 and (**S1E**), semi-quantitative RT-PCR analysis to observe expression of "rosette-specific" genes of *DACH1* and *PLZF*, while no expressions were detected in hiPSC cells.

Supplementary Figure S2.

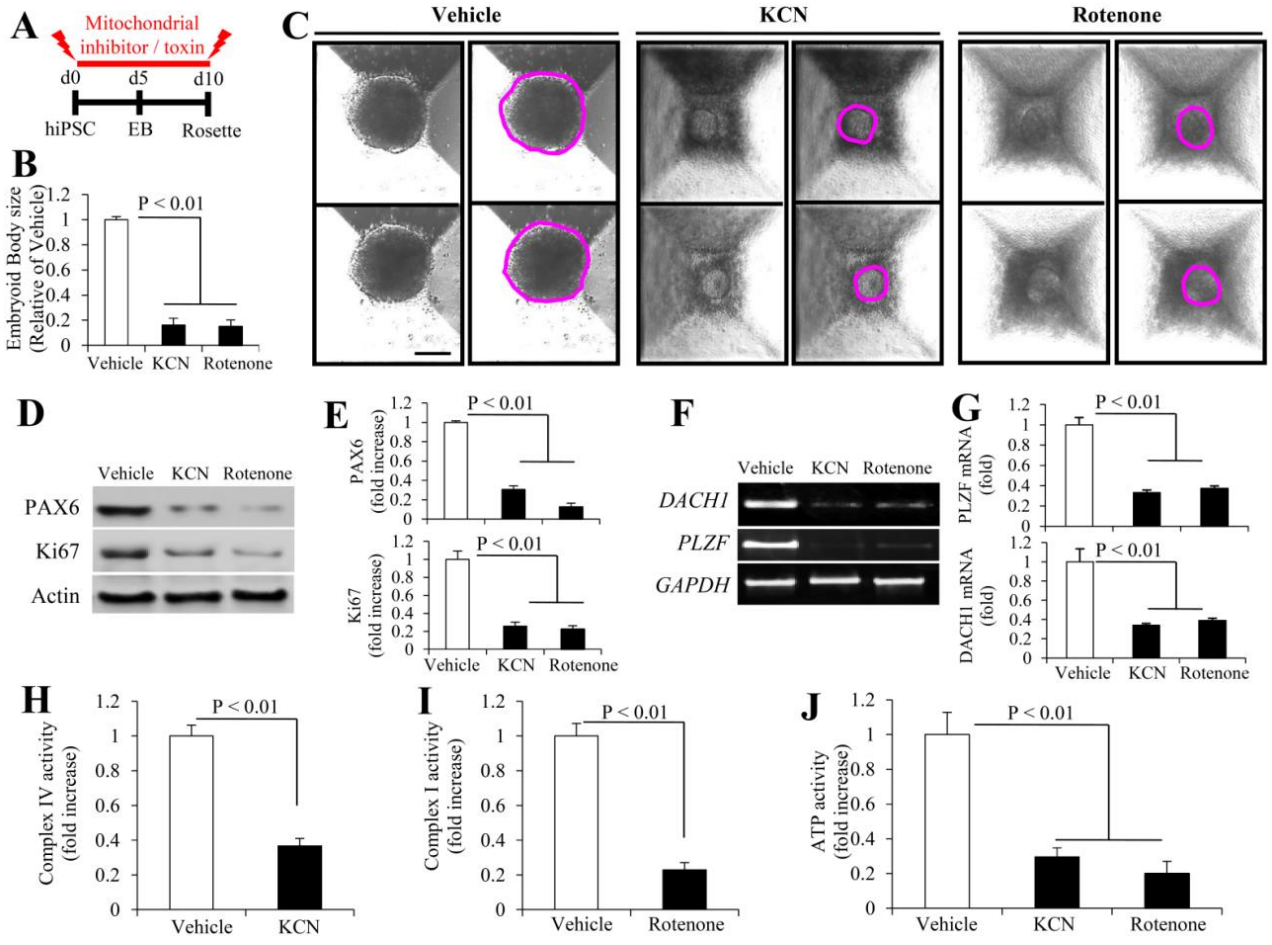

Figure S2 (Related to results: Effect of mitochondrial function on DA neuron-directed differentiation). Effects of KCN and rotenone on EB and rosette formations.

(**S2A**) A schematic representation of the neural EB and rosette formations under KCN or rotenone treatments. (**S2B**) Quantification of EB morphology shown in **S2C** (n = 3 independent experiments; mean ± SEM. 10 EBs in each group were traced per experiment). (**S2D-E**) immunoblotting analysis to detect PAX6 and Ki67. Representative immunoblots for PAX6, Ki67 and β-actin. Data are expressed as fold increase relative to vehicle rosette (**S2E**). β-actin was used as a protein loading control (n = 3 independent experiments; mean ± SEM). (**S2F-G**), semi-

quantitative RT-PCR analysis to observe expression of "rosette-specific" genes of *DACH1* and *PLZF*. Representative semi-quantitative RT-PCR images for *DACH1*, *PLZF* and *GAPDH* (**S2F**). Data are expressed as fold increase relative to vehicle rosette (**S2G**). *GAPDH* was used as a control (n = 3 independent experiments; mean ± SEM). Enzymatic activity of complex IV (**H**), I (**I**), and cellular ATP levels (**J**) were determined in cell lysates from rosette with or without KCN and rotenone treatments. Data are expressed as fold increase relative to vehicle rosette (n = 3 independent experiments; mean ± SEM). Scale bar, 200µm. Statistical analysis was performed using Statview software (SAS Institute, Version 5.0.1). For **B**, **E, G** and **J**, one-way ANOVA was used for repeated measure analysis, followed by Fisher's protected least significant difference for post hoc comparisons. Student's *t* test was used for **H** and **I**.

Supplementary Video S1. (Related to figure 4E-J and figure 6M-R). Mitochondrial movement in the neurites of hiPSC-derived DA neurons with different treatments.

Videos S1A-C: mitochondrial movement in the neurites of hiPSC-derived DA neurons differentiated for 10 days (**Video S1A)**; 15 days (**Video S1B**) and 20 days (**Video S1C**). In the neuronal process of hiPSC-derived DA neurons differentiated for 15 (**Video S1B**) and 20 days (**Video S1C**), mitochondria showed elongated morphology and movement with significantly higher speed and longer travel distance. **Videos S1D-F**: mitochondrial movement in the neurites of hiPSC-derived DA neurons differentiated for 20 days (**Video S1D**) with or without KCN (**Video S1E**) or rotenone (**Video S1F**) treatments, mitochondria showed shortened morphology and significantly less movement.

Supplemental Experimental Procedures

Immunoblotting analysis

Differentiated cells cultured in DA neuronal differentiation medium for 5, 10, 15 and 20 days or the rosettes were washed with ice-cold PBS and proteins extracted with 150μl of lysis buffer. After centrifugation at 12,000 × g for 10 min at 4°C, we collected the supernatant and determined protein concentrations; we boiled 30 μg proteins in protein loading buffer for 5 min, separated the proteins on a 10% SDS polyacrylamide gel, and subsequently transferred to nitrocellulose membranes. Nonspecific binding was inhibited by incubation in TBST (20 mM Tris-buffered saline with 0.1% Tween 20, pH 7.5) containing 5% nonfat dried milk for 1 hour at room temperature. Membranes were incubated with the following primary antibodies: Rabbit anti-PAX6 (1:1000, 42-6600, Invitrogen), mouse anti-Ki67 (1:1000, 556003, BD Pharmingen™), Rabbit anti-Oct-4 (Octamer-binding transcription factor 4, 1:1000, Life Technologies), Rabbit anti-TH (tyrosine hydroxylase, 1:2000, Chemicon, Temecula, CA), mouse anti-TuJ1 (class III β-tubulin, 1:10000, Sigma), and rabbit anti-syn (synaptophysin, 1:5000, A0010, Dako) overnight at 4°C. After three washes with TBST, membranes were incubated for 2 h with horseradish (HRP)-conjugated secondary antibodies (Pierce Chemical Company, USA) and developed using enhanced chemiluminescence (ECL Amersham Biosciences, England). To ensure equal protein loading of the samples, the same membrane was probed with anti-mouse β-actin monoclonal antibody (Sigma-Aldrich, MO) at a 1:10,000 dilution.

Immunocytochemistry

The BM2-3 hiPSCs, at 16 passages, the induced DA neurons, after differentiation for 5, 10, 15 and 20 days, or the attached neural aggregates, all cultured on coverslips, were fixed with 4% ice-cold paraformaldehyde for 5 min and then permeabilized with PBS containing 0.1% Triton

and 5% goat serum for 1 h followed by incubation with the following primary antibodies: rabbit anti-Oct4 (1:2500, A13998, Life Technologies) and mouse anti-Nanog (1:2500, ab173368, abcam); rabbit anti-SOX2 (1:2500, A13992; Life Technologies) and rat anti-SSEA3 (1:500, 41-4400, Life Technologies); Rabbit anti-PAX6 (1:1000, 42-6600, Invitrogen) and mouse anti-Ki67 (1:1000, 556003, BD Pharmingen™); rabbit anti-TH (1:2000, Chemicon, Temecula, CA) and mouse anti-TuJ1 (1:10000, Sigma), or rabbit anti-TH (1:2000, Chemicon, Temecula, CA) and mouse anti-Syn IgG (1:1000, chemicon) at 4°C for 16 h. Cells were incubated with Alexa Fluor 488-conjugated goat anti-rabbit IgG and 594 goat anti-mouse/rat IgG (1: 1000, Invitrogen) or Alexa Fluor 594-conjugated goat anti-rabbit IgG and 488 goat anti-mouse IgG (1: 1000, Invitrogen) for 1 h at room temperature. After washing with PBS, neurons were covered with Vectashield mounting medium (H-1000, Vector Laboratories). Images were acquired (equal exposure for all groups) using confocal microscopy (Leica) and analyzed using the Universal Metamorph Image Program.

We measured synaptic density of cultured neurons by counting the number of synaptophysin-positive clusters in neuronal dendrites and puncta per 100 microns of TH positive dendrite (presented as the number of synaptophysin clusters per 100 microns of dendrite) and calculated by dividing the length of the TH+ dendrites.

Real-time PCR measurement

RNA was extracted identified cells by using TRIzol reagents (Invitrogen, Carlsbad, CA, USA) according to the manufacturer's protocol as described in our previous study (Fang et al., 2015). cDNA was directly proformed using TaqMan reverse transcription reagents kit (Applied Biosystems, Foster City, CA, USA). Total RNA (1 μg) was used for the synthesis of cDNA with TaqMan Reverse Transcription Reagents kit (Roche Applied Biosystems). Real time-PCR was

performed on an ABI Prism 7900 Sequence Detection System (Applied Biosystems) with TaqMan PCR Master Mix. Semi-quantitative PCR was performed in the GeneAmp PCR System 2720 (Applied Biosystems), and same volume of reaction products are electrophoresed on an agarose gel. The sequences of the primers were EN1 (Hs00154977_m1, Thermo Fisher), OTX2 (Hs00222238_m1, Thermo Fisher), FOXA2 (Hs00232764_m1, Thermo Fisher), map2 (Hs00258900_m1, Thermo Fisher), DDC (AADC) (Hs01105048_m1, Thermo Fisher), SLC18A2 (VMAT2) (Hs00996835_m1, Thermo Fisher), LMX1A (Hs00892663_m1, Thermo Fisher), SLC6A3 (DAT) (Hs00997374_m1, Thermo Fisher), ZBTB16 (PLzf) (Hs00957433_m1, Thermo Fisher), DACH1 (Hs00362088_m1, Thermo Fisher).

Electrophysiology analysis

Electrophysiologic experiments were performed on day-10, -15 and -20 differentiated DA neurons. Electrophysiology recordings were performed as described previously (Vierbuchen et al., 2010). We analyzed cells at indicated times after induction, recording resting membrane potential as well as spontaneous and evoked action potentials using current clamp whole-cell configuration. Evoked action potentials were recorded at a holding potential on resting membrane potential; step currents ranging from -10 pA to +90 pA were injected at 20 pA to elicit action potentials. Whole-cell currents including sodium currents and potassium currents were recorded at a holding potential of -70 mV, with voltage steps ranging from -70 mV to +50 mV delivered at 10 mV increments. Spontaneous postsynaptic currents (sPSCs) were recorded at a holding potential of -70 mV with voltage clamp configuration. The pipette solution for patch-clamp experiments contained (in mM) 130 K-gluconate, 10 KCl, 5 $MgCl_2$, 5 HEPES, 0.6 EGTA, 0.06 $CaCl_2$, 2 MgATP, and 0.2 Na_2GTP, pH adjusted to 7.2 with KOH. The recording bath solution contained (in mM) 119 NaCl, 5 KCl, 20 HEPES, 30 glucose, 2 $CaCl_2$ and 2 $MgCl_2$, pH

adjusted to 7.3 with NaOH. We acquired whole-cell patch clamp recordings using a MultiClamp 700B amplifier, Digidata 1440A, and Clampex data acquisition software (Molecular Devices) at room temperature.

Measurement of respiratory chain complex enzyme activities and ATP levels

Enzyme activities in complex I (NADH-ubiquinonereductase), complex IV (cytochrome c oxidase, CcO), and ATP levels were determined as described previously (Gan et al., 2014a). The reaction was then initiated by the addition of 50 µl of ferrocytochrome substrate solution (0.22 mM) and changes in absorbance of cytochrome c at 550 nm were measured using a Shimadzu (Kyoto, Japan) UV1200 spectrophotometer. Activity is expressed as micromoles of cytochrome oxidized per min^{-1} mg^{-1} protein using an extinction coefficient of 18.64 mM^{-1} cm^{-1}.

ATP levels were determined using an ATP Bioluminescence Assay Kit (Roche) following the manufacturer's instructions (Du et al., 2008; Du et al., 2010). Briefly, cells were harvested using the provided lysis buffer, incubated on ice for 15 minutes, and centrifuged at 13,000g for 10 minutes. ATP levels were measured using a Luminescence plate reader (Molecular Devices) with an integration time of 10 seconds.

Determination of mitochondrial membrane potential (ΔΨ) with TMRM and Mitochondrial ROS generation with Mitosox Red

Differentiated neuronal cells were seeded at low density onto Lab-Tek eight-well chamber slides (10,000 cells /well). Mitochondrial ROS generation was determined using MitoSox Red (Invitrogen), a unique fluorogenic dye highly selective for detection of superoxide production in live cell mitochondria (Gan et al., 2014a; Gan et al., 2014b; Iuso et al., 2006; Polster et al., 2014; Xu and Chisholm, 2014). Cells were incubated with fresh medium containing 2.5 µM MitoSox for 30 min at 37°C. To detect mitochondrial membrane potential, cells were co-stained with

TMRM (100nM; Invitrogen) for 30 min and MitoTracker Green (MTGreen, 100nM, Invitrogen). In addition, mitochondria were labeled with Mitotracker Red (MTRed, 100nM, Invitrogen) for 30 min at 37 °C before fixation to visualize morphology. Fluorescence images were acquired on a Leica SP5 confocal microscope and analyzed using Leica LAS AF software (Leica Wetzlar). Excitation wavelengths were 543 nm for MitoSox, TMRM or MTRed, and 488nm for MTGreen, respectively. Fluorescent signals were quantified using NIH Image J software. We used MetaMorph (Molecular Devices) and NIH Image J software for quantification and measurement of fluorescent signals of mitochondrial length and mitochondrial density. Mitochondrial size, shape, density, and fluorescent intensity were quantified by an investigator blinded to experimental groups. Mitochondria from 20-25 randomly selected cells were measured and quantified.

Evaluation of intracellular ROS levels

Intracellular ROS levels were accessed by election paramagnetic resonance (EPR) spectroscopy as described in our previous study (Fang et al., 2015; Fang et al., 2016). CMH (cyclic hydroxylamine 1-hydroxy-3-methoxycarbonyl-2, 2, 5, 5-tetramethyl-pyrrolidine, 100μM) was incubated with cultured cells for 30 min and then washed with cold PBS. The cells were collected and homogenized with 100 μl of PBS for EPR measurement. The EPR spectra were collected, stored, and analyzed with a Bruker EleXsys 540 x-band EPR spectrometer (Billerica, MA) using the Bruker Software Xepr (Billerica, MA).

Axonal mitochondrial trafficking recording and data analysis in differentiated neuronal cells

These recordings were performed using previously reported protocols (Du et al., 2010; Guo et al., 2013). Axonal mitochondria were visualized following transfection with pDsRed2-mito (Clontech) in differentiated neuronal cells using lipofectamine LTX and plus regent (Invitrogen)

according to the manufacturer's protocol. Three to four days after transfection, time-lapse recordings of labeled mitochondrial movement were acquired on a Carl Zeiss (Axiovert 200) microscope with incubation system (PeCon) to maintain differentiated neuronal cells at 37°C during image collection. Collection of image stacks and velocity measurements were made using the AxioVision Software as previously described (Du et al., 2010; Guo et al., 2013). For standard recordings, images of mitochondria in one process per differentiated neuronal cell were collected every 3 s for 2 min. Only the proximal segment of the axon was acquired and recorded.

Mitochondria in each frame of every video recording were individually tracked using AxioVision Software and the average velocity was calculated during the 2-min recording period. The average velocity of every mitochondrion in one measured process in each cell was then averaged to obtain the average velocity for mitochondrial movement per process. In addition, the percentage of movable mitochondria, mitochondrial total traveling distance (total distance traveled irrespective of direction during the recording period), single mitochondrial length and mitochondrial density in each process were all determined according to previous studies with modifications (Gan et al., 2014a; Trimmer and Borland, 2005). Exposure periods (30–50 ms) were kept at a minimum to limit phototoxicity.

Statistical analysis

Statistical analysis was performed using Statview software (SAS Institute, Version 5.0.1). One-way ANOVA or Student's *t* test was used for repeated measure analysis, followed by Fisher's protected least significant difference for post hoc comparisons. Data are presented as mean ± SEM. $P < 0.05$ was considered significant.

Supplemental References

Du, H., Guo, L., Fang, F., Chen, D., Sosunov, A.A., McKhann, G.M., Yan, Y., Wang, C., Zhang, H., Molkentin, J.D., *et al.* (2008). Cyclophilin D deficiency attenuates mitochondrial and neuronal perturbation and ameliorates learning and memory in Alzheimer's disease. Nature medicine *14*, 1097-1105.

Du, H., Guo, L., Yan, S., Sosunov, A.A., McKhann, G.M., and Yan, S.S. (2010). Early deficits in synaptic mitochondria in an Alzheimer's disease mouse model. Proceedings of the National Academy of Sciences of the United States of America *107*, 18670-18675.

Fang, D., Wang, Y., Zhang, Z., Du, H., Yan, S., Sun, Q., Zhong, C., Wu, L., Vangavaragu, J.R., Yan, S., *et al.* (2015). Increased neuronal PreP activity reduces Abeta accumulation, attenuates neuroinflammation and improves mitochondrial and synaptic function in Alzheimer disease's mouse model. Human molecular genetics *24*, 5198-5210.

Fang, D., Zhang, Z., Li, H., Yu, Q., Douglas, J.T., Bratasz, A., Kuppusamy, P., and Yan, S.S. (2016). Increased Electron Paramagnetic Resonance Signal Correlates with Mitochondrial Dysfunction and Oxidative Stress in an Alzheimer's disease Mouse Brain. Journal of Alzheimer's disease : JAD *51*, 571-580.

Gan, X., Huang, S., Wu, L., Wang, Y., Hu, G., Li, G., Zhang, H., Yu, H., Swerdlow, R.H., Chen, J.X., *et al.* (2014a). Inhibition of ERK-DLP1 signaling and mitochondrial division alleviates mitochondrial dysfunction in Alzheimer's disease cybrid cell. Biochim Biophys Acta *1842*, 220-231.

Gan, X., Wu, L., Huang, S., Zhong, C., Shi, H., Li, G., Yu, H., Howard Swerdlow, R., Xi Chen, J., and Yan, S.S. (2014b). Oxidative stress-mediated activation of extracellular signal-regulated kinase contributes to mild cognitive impairment-related mitochondrial dysfunction. Free radical biology & medicine *75*, 230-240.

Guo, L., Du, H., Yan, S., Wu, X., McKhann, G.M., Chen, J.X., and Yan, S.S. (2013). Cyclophilin D deficiency rescues axonal mitochondrial transport in Alzheimer's neurons. PloS one *8*, e54914.

Iuso, A., Scacco, S., Piccoli, C., Bellomo, F., Petruzzella, V., Trentadue, R., Minuto, M., Ripoli, M., Capitanio, N., Zeviani, M., *et al.* (2006). Dysfunctions of cellular oxidative metabolism in patients with mutations in the NDUFS1 and NDUFS4 genes of complex I. The Journal of biological chemistry *281*, 10374-10380.

Polster, B.M., Nicholls, D.G., Ge, S.X., and Roelofs, B.A. (2014). Use of potentiometric fluorophores in the measurement of mitochondrial reactive oxygen species. Methods in enzymology *547*, 225-250.

Trimmer, P.A., and Borland, M.K. (2005). Differentiated Alzheimer's disease transmitochondrial cybrid cell lines exhibit reduced organelle movement. Antioxidants & redox signaling *7*, 1101-1109.

Vierbuchen, T., Ostermeier, A., Pang, Z.P., Kokubu, Y., Sudhof, T.C., and Wernig, M. (2010). Direct conversion of fibroblasts to functional neurons by defined factors. Nature *463*, 1035-1041.

Xu, S., and Chisholm, A.D. (2014). C. elegans epidermal wounding induces a mitochondrial ROS burst that promotes wound repair. Developmental cell *31*, 48-60.